

Shakebot: A Low-cost, Open-source Shake Table for Ground Motion Seismic Studies

Zhiang Chen, Devin Keating, Yash Shethwala, Aravind Adhith Pandian Saravanakumaran,
Ramon Arrowsmith, Chris Madugo, Albert Kottke, Jnaneshwar Das

Abstract—Our earlier research built a virtual shake robot in simulation to study the dynamics of precariously balanced rocks (PBR), which are negative indicators of earthquakes in nature. The simulation studies need validation through physical experiments. For this purpose, we developed *Shakebot*, a low-cost (under \$2,000), open-source shake table to validate simulations of PBR dynamics and facilitate other ground motion experiments. The Shakebot is a custom one-dimensional prismatic robotic system with perception and motion software developed using the Robot Operating System (ROS). We adapted affordable and high-accuracy components from 3D printers, particularly a closed-loop stepper motor for actuation and a toothed belt for transmission. The stepper motor enables the bed to reach a maximum horizontal acceleration of 11.8 m/s^2 (1.2 g), and velocity of 0.5 m/s , when loaded with a 2 kg scale-model PBR. The perception system of the Shakebot consists of an accelerometer and a high frame-rate camera. By fusing camera-based displacements with acceleration measurements, the Shakebot is able to carry out accurate bed velocity estimation. The ROS-based perception and motion software simplifies the transition of code from our previous virtual shake robot to the physical Shakebot. The reuse of the control programs ensures that the implemented ground motions are consistent for both the simulation and physical experiments, which is critical to validate our simulation experiments.

I. INTRODUCTION

For decades, researchers have used mechanical earthquake simulators, also known as shake tables, for ground motion seismology research and education [1, 2, 3]. An important application of shake tables is to study the dynamics of precariously balanced rocks (PBRs), which are free-standing rocks balanced on, but not attached to sub-horizontal pedestals [4, 5, 6]. Because an earthquake of significant magnitude would topple PBRs, the fragile configurations of PBRs provide upper-bound constraints on ground motions, refining probabilistic seismic hazard analysis [7, 8].

The dynamics of the PBR overturning process are non-linear. Purvance et al. [9] used a shake table to study the PBR overturning dynamics. However, difficulties can arise when using conventional shake tables to repeat overturning experiments. For example, when analyzing PBR fragility, shake experiments would involve accurate and repeated positioning of a large boulder on the shake table to record the overturning responses given ground motions. These boulders are often so heavy that the use of a crane or forklift is needed, and repositioning them precisely is difficult (e.g., [10]), complicating experiment repeatability.

In an effort to reduce variability and to automate these PBR overturning analyses, our previous study developed a virtual shake robot in simulation [11]. The virtual shake robot

utilized core technologies in robotics, such as Robot Operating System (ROS), Gazebo simulation toolbox, and Bullet physics engine. Although the virtual shake robot allows us to conduct shake experiments in simulation, the results need to be validated through physical experiments for a thorough understanding of PBR dynamics. To complete this validation, we designed and built a low-cost, small-scale shake table, called Shakebot. By leveraging robotics tools, this platform can achieve cosine displacement ground motions, as well as a recreation of motions recorded from actual earthquakes. The Shakebot enables us to reproduce the shake experiments to validate the PBR overturning simulation.

The Shakebot provides a reverse method for simulation validation. Physics engines have been used for robotic development. However, when robotic systems are transitioned from simulations to the real world, simulation gaps may cause critical failures (e.g., in the arena of reinforcement learning [12, 13]). When using a physics engine for scientific studies, we also need to address the simulation gap to calibrate and scale-up the simulation experiments. Using the Shakebot, we test the overturning dynamics of down-scaled, 3D-printed PBRs. We build the same PBR models in simulation and validate the overturning dynamics using our virtual shake robot. Following this approach, we are able to compare the overturning patterns obtained from the Shakebot and the virtual shake robot, further allowing us to quantify the uncertainty in simulation. The Shakebot serves as a validation tool for simulation studies, aiding in learning more about the real-time dynamics of the PBRs and potentially calibrating physics engine parameters to reduce the simulation gaps.

The Shakebot demonstrates interdisciplinary research in the use of automated robotic systems for geoscience studies, enhancing the impact of robotics in the natural sciences. Besides its contribution to seismology, the key technical contributions of this paper are as follows.

- It is the first shake table developed based on robotic concepts (perception and motion systems) and tools (ROS). Because of using ROS, the control systems are reused from our previous virtual shake robot, ensuring that the ground motions (the motion of the bed) are consistent in physical and simulation experiments. This consistency is vital for simulation validation.
- The hardware mechanism is simplified by design. The Shakebot adopts a closed-loop stepper motor with a toothed belt and pulley transmission mechanism. Most of the mechanical parts and components are off-the-

	Availability	Cost (USD)	Payload (kg)	Vel (m/s)	Acc (g)	Software	Programmable	Transmission
Quasner [14]	proprietary	NA	7.5	0.399	2.5	NA	✓	ball screw
CUSHAKE [15]	proprietary	45000	3500	0.01	1	DEPSIM	✓	threaded rod
Kelvin [16]	proprietary	1250	NA	NA	NA	NA	×	reciprocating arm
SARSAR [17]	open source	770	200	0.35	1.5	NA	✓	ball screw
Shao and Enyart [18]	proprietary	NA	228	NA	4	NA	✓	hydraulic actuators
Kınay [19]	open source	NA	80	0.25	2	Scilab	✓	ball screw
Testbox shaketable [20]	proprietary	NA	50	0.5	1	TESTLAB	✓	ball screw
Shakebot (ours)	open source	1300	2	0.5	1.2	ROS	✓	toothed belt

TABLE I: Shake tables and their specifications.

shelf, and only a few parts are 3D-printed. The simplified design lowers costs and expedites prototyping. Additionally, for safety anticipation, we employ a double-emergency mechanism to allow system override in case of malfunction.

- Compared with traditional shake tables that only use accelerometers, our Shakebot also leverages a top-down view camera to estimate ground motion. The perception system fuses accelerations and camera-based displacements for better ground velocity estimation.
- We have open-sourced our hardware and software to promote robotic applications in seismic research and education: https://github.com/DREAMS-lab/asu_shake_table.

The paper is structured as follows. In Sec. II, we discuss commercial and academic shake tables available for civil engineering and seismology, and highlight a few of their limitations. From Sec. III to Sec. VI, we describe the mechanical design, the perception system, the motion system, and the calibration system. In Sec. VII, we discuss the results of our experiments, followed by our conclusions and future directions in Sec. VIII.

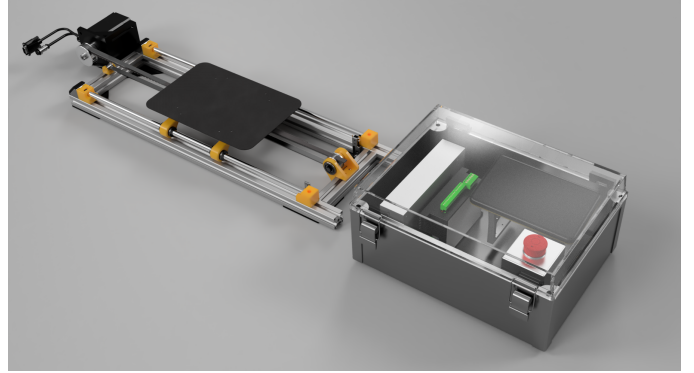
II. RELATED WORK

Existing commercially available shake tables [14, 21] are comparatively expensive, making them less accessible for research. Academically accessible alternatives are either too massive [15], taking ample space to install, or only allow a fixed ground motion pattern [16]. The existing shake table solutions are unsatisfactory to the academic community because of limited options for open-source, low-cost devices that can provide programmable ground motions. TABLE I shows the comparison between existing shake tables and the Shakebot.

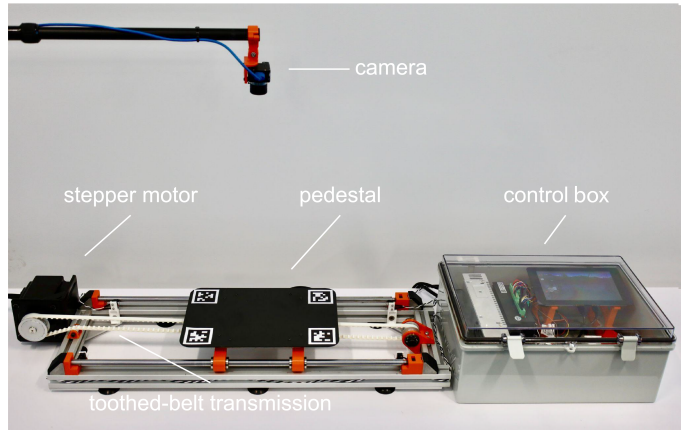
Another limitation of existing shake tables is that they solely employ accelerometers to measure ground motion. Because accelerometers are affected by high-frequency noise and velocity (usually integrated from the acceleration) drifts over time, it is difficult to quantify the uncertainties introduced by these filters, without additional exteroceptive sensors such as a motion capture system, or cameras.

III. SYSTEM DESCRIPTION

In this section, we discuss the mechanical design, motor selection strategy, and safety mechanism. The system is designed to satisfy the ground motion requirements—maximum



(a) Shakebot CAD model



(b) Shakebot experimental setup

Fig. 1: Shakebot CAD model and actual experimental setup. Stepper motor actuates pedestal through toothed belt and pulley transmission. Control box includes power supply, stepper motor drive, Raspberry Pi, emergency push button, and touchscreen.

dynamic acceleration of 11.8 m/s^2 (1.2 g), maximum velocity of 0.5 m/s , and maximum PBR payload mass of 2 kg .

A. Hardware Mechanism

Two main components of the Shakebot are a chassis and a control box, as shown in Fig. 1. The chassis is constructed of an extruded aluminum T-slot frame that supports two linear shafts. A carriage is mounted on the linear shafts with ball bearings, which reduce the friction between the linear shafts and the carriage. A flatbed (pedestal) is attached to the carriage to hold scale-model PBRs. A stepper motor (i.e., NEMA 34) actuates the carriage through a toothed belt and

pulley transmission. The stepper motor controller, contained in the control box, drives this stepper motor. The control box also houses the power supply (S-350-60), stepper motor drive (CL86T), an emergency stop button, a touchscreen for the user interface, and a Raspberry Pi that serves as the processing unit and handles trajectory generation and low-level system control.

B. Motor Selection

To select a stepper motor, we considered the stepper motor torque at its maximum angular velocity to satisfy the required ground motion acceleration and velocity. Because stepper motor torque decreases with velocity, if the torque at the maximum velocity satisfies the acceleration requirement, the stepper motor can also achieve so at any smaller velocities. We selected Nema 34HS31, a closed-loop stepper motor (with an encoder) with a torque output of 1.56 Nm at the maximum speed of 1200 RPM. The maximum translational force is calculated from the torque,

$$F = ma = \frac{\tau}{r} \quad (1)$$

where F is the translational force, r is the outside radius of the toothed pulley, m is the maximum payload mass (including carriage and PBR), a is the maximum translational acceleration, and τ is the stepper motor torque. We select a toothed pulley with an outside radius of 25.91 mm . The translational force at the maximum speed is 60.21 N . Considering a maximum total payload mass m of 4 kg (including a 2 kg carriage and 2 kg PBR), the corresponding acceleration produced from the translational motion is 15.1 m/s^2 (1.54 g). The ratio of the calculated acceleration to the required acceleration is 1.28, which was found to be enough empirically to compensate for the friction and energy losses in transmission. Additionally, at the maximum stepper motor speed of 1200 RPM, the translational speed can reach 0.52 m/s , which also satisfies our design requirement for PBR studies. Note that we used the outside radius on the specifications of the toothed pulley for the calculation here. The outside radius value is adequate for the stepper motor selection. We conducted a calibration process that uses a camera and several fiducial markers to estimate this radius precisely for more accurate control. The calibration process is discussed in Sec. VI-B.

C. Safety Mechanism

The design incorporates two levels of safety features. The first level consists of a pair of limit emergency switches situated at either end of the carriage's range of motion, as shown in Fig. 2. These switches link to the emergency stop function on the stepper motor drive. Once either of these switches is triggered, the stepper motor is disabled. The second level of protection is supplied by an emergency push button in the control box, which disconnects the power supply from the stepper motor drive. The emergency push button can be manually activated by the Shakebot's operator. Fig. 2 shows a top-down view of the Shakebot.

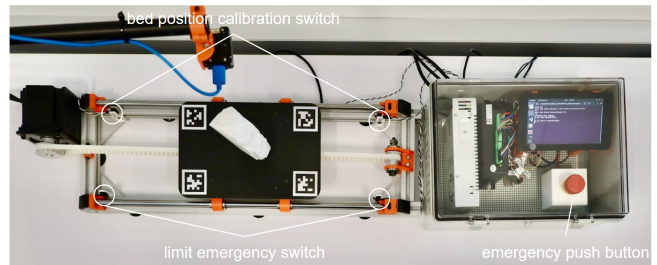


Fig. 2: Shakebot from top-down view illustrating double emergency mechanism.

IV. PERCEPTION SYSTEM

The perception system estimates the status of the bed using a camera and an accelerometer. As shown in Fig. 1b and Fig. 2, four fiducial markers are affixed to the corners of the bed. A top-down view FLIR Chameleon[®]3 Color Camera CM3-U3-13Y3C-CS 1/2" captures the position and orientation of the bed using the *apriltag_ros* ROS package [22, 23]. Additionally, an accelerometer (Wit Motion HWT905-TTL) attached underneath the bed measures acceleration (ground motion acceleration). We directly obtain ground motion displacement and acceleration from the fiducial marker detection and accelerometer, respectively. We additionally estimate the ground motion velocities by fusing the information from the fiducial marker detection and accelerometer.

A. Displacement Estimation

The camera estimates ground motion displacement by detecting the fiducial markers at each corner of the bed. The *apriltag_ros* package provides the pose of each visible marker in the camera coordinates. When the bed moves from one position to another, we obtain the relative pose of a marker attached to the bed,

$$H_i^j = H_c^j \cdot H_i^c = [H_c^c]^{-1} \cdot H_i^c \quad (2)$$

where i and j indicate marker positions at two time stamps, c indicates the camera coordinates, H_a^b is the transformation matrix for position a with respect to position b . H_i^c and H_j^c are obtained using the *apriltag_ros* package.

We extract the translation vector from H_i^j as the relative displacement of the fiducial marker at two positions. We estimate ground motion displacement by averaging the relative displacements from all visible fiducial marker detections. When a fiducial marker is obstructed by a PBR, the ground motion displacement estimation only relies upon the remaining visible fiducial markers. Note that the relative displacement from *apriltag_ros* is inaccurate despite intrinsic camera calibration. To address this issue, a process of perception calibration is presented in Sec. VI-A.

B. Acceleration Estimation

The accelerometer attached at the bottom of the bed measures the vector of ground motion acceleration in three dimensions. The bed, however, has one degree-of-freedom prismatic motion. To obtain the acceleration along the bed

movement direction, we align x-axis of the accelerometer with the bed movement direction. However, the manual alignment cannot be perfect. We additionally calculate the Euclidean distance of acceleration vector to obtain the absolute acceleration, which is also the value of the acceleration vector along the bed movement direction. To remove high-frequency vibration, we apply a low-pass filter to the raw acceleration data.

C. Velocity Estimation

We estimate ground motion velocity by fusing the derived velocities from the fiducial marker detection and accelerometer data. Fig. 3 illustrates the velocity fusion process. During a shake experiment, the timestamped ground motion displacements and accelerations are recorded. After the shake experiment, we implement numerical derivation to obtain velocity from the ground motion displacements,

$$v_d(t) = \frac{d(t) - d(t-1)}{\Delta t} \quad (3)$$

where $v_d(t)$ is the velocity derived from displacement at time t , and $d(t)$ is the ground motion displacement at time t . From the ground motion accelerations, we conduct numerical integration to obtain velocity,

$$v_a(t) = \frac{1}{2}(a(t) + a(t-1))\Delta t \quad (4)$$

where $v_a(t)$ the velocity derived from acceleration at time t , and $a(t)$ is the ground motion acceleration at time t .

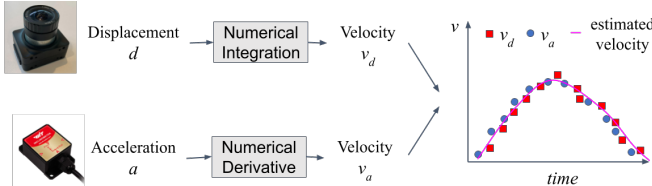


Fig. 3: Velocity fusion workflow. Estimated velocity is regression of velocities from displacement and acceleration.

We phrase the ground motion velocity estimation as a regression problem where an objective function needs to be found to minimize its distance to all velocities derived from ground motion displacements and accelerations,

$$\hat{v}(t) = \arg \min_{\theta} \|f(t; \theta) - v_s(t)\| \quad (5)$$

where $\hat{v}(t)$ is the estimated ground motion velocity, $f(t; \theta)$ is a parametric objective function, and $v_s \in \{v_d(t)\} \cup \{v_a(t)\}$. Note that $\{v_d(t)\}$ and $\{v_a(t)\}$ are not synchronized. The fiducial marker detection and accelerometer have different frame rates. When they happen to have the same time stamps, we calculate their average as $v_s(t)$. The objective function $f(t; \theta)$ has many options. We select the 3rd order polynomial function for demonstration in Sec. VII.

V. MOTION SYSTEM

The Shakebot has a hierarchical motion system and a user interface (UI) to facilitate shake experiments. The hierarchical motion system provides two options to emulate the motion: single-pulse cosine displacement motion and realistic ground motion from the seismometer. The UI assists users in repeating the shake experiment where single-pulse cosine displacement motions are deployed with different ground motion parameters.

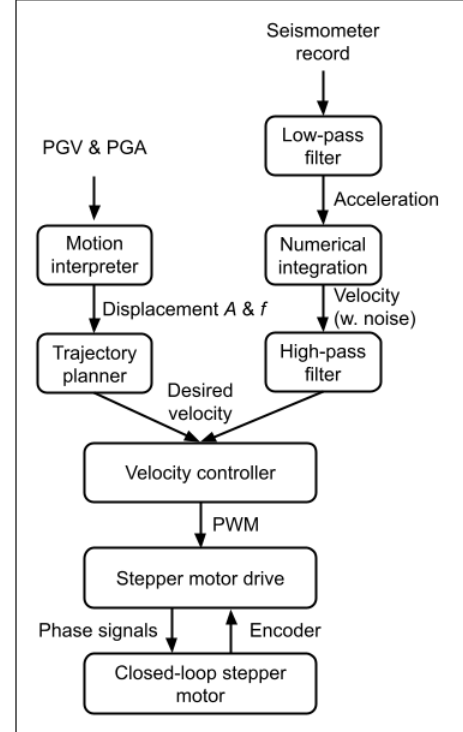


Fig. 4: Motion system.

A. Motor Control

The Shakebot motion is enabled by a hierarchical motion planner in the Raspberry Pi, which outputs PWM signals to the closed-loop stepper motor drive. Fig. 4 shows the hierarchical motion system. The first ground motion option is a single-pulse cosine displacement,

$$d(t) = A - A \cos(2\pi ft), \quad (6)$$

where $d(t)$ is the ground displacement function, A is the amplitude, f is the frequency, and $t \in [0, 1/f]$ is time. A and f are derived from ground motion parameters,

$$f = \frac{1}{2\pi\kappa} \quad (7)$$

$$A = \frac{\alpha g}{4\pi^2 f^2} \quad (8)$$

where α is the peak ground acceleration (PGA), κ is the ratio of peak ground velocity to peak ground acceleration (PGV/PGA), and g is the gravitational acceleration. As shown in Fig. 4, the motion interpreter converts (PGV, PGA)

to (A, f) using Eqs. 7-8. With (A, f) , the trajectory planner takes derivative of the cosine displacement function to obtain ground velocity function,

$$v(t) = 2\pi A f \sin(2\pi f t) \quad (9)$$

where $v(t)$ is the ground velocity function, and $t \in [0, 1/f]$ is time. From the ground velocity function, we uniformly sample velocity points $\{v\}$ as the input of the velocity controller. The sampling frequency is a user-defined parameter (usually 200 Hz). Note that the velocity commands $\{v\}$ are desired translational velocities of the bed. The velocity controller converts the translation velocity to the angular velocity of the stepper motor,

$$\omega(t) = \frac{v(t)}{r} \quad (10)$$

where $\omega(t)$ is angular velocity for the stepper motor, and r is the radius of the toothed pulley. The angular velocity commands are further converted to PWM signals for the input of the stepper motor drive, stepper motor, and encoder attached to the stepper motor form a closed-loop control to execute the PWM signals.

Besides the cosine ground displacement function, the Shakebot also supports ground motion recreation from real seismometer records. As shown in Fig. 4, we first implement a low-pass filter to remove the high-frequency noises in the raw acceleration data. The numerical integration produces velocities from the accelerations. Then we have a high-pass filter to remove the low-frequency noises in the velocities, because the low-frequency noises in velocities may cause accumulated displacement errors. Note that the output of the high-pass filter is a set of velocities $\{v\}$, which have the same format as the output from the trajectory planner. Because both the trajectory planner and high-pass filter had the same output format, we share a velocity controller to process the desired velocity commands.

B. Control User Interface

The UI is a portal through which users conduct shake experiments to study PBR overturning responses. Fig. 5 shows the workflow of the UI. Once initialized, the UI prompts the user to place a PBR on the bed. Then the user needs to input (PGV/PGA, PGA), which is converted to (PGV, PGA). The motion module (Fig. 4) executes a single-pulse cosine displacement ground motion based on the (PGV, PGA). After the ground motion is completed, the UI prompts the user to input the overturning response of the PBR (i.e., being toppled or remaining balanced). The overturning responses with ground motion parameters and perception estimates are saved in a CSV file.

VI. SYSTEM CALIBRATION

The Shakebot needs to be calibrated before conducting the shake experiments. We first calibrate the camera intrinsics and fiducial marker detection, and this calibrated perception system is used to facilitate velocity controller calibration.

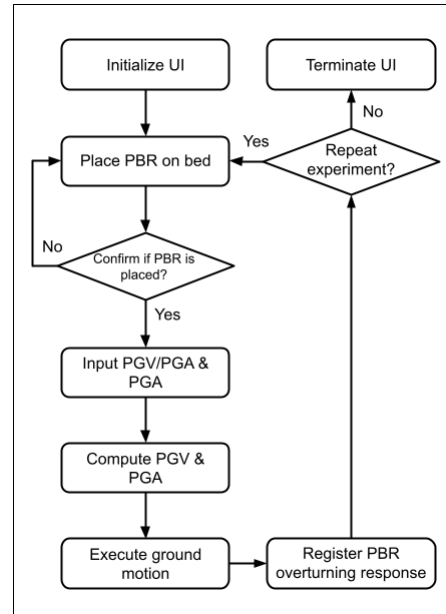


Fig. 5: User interface workflow.

A. Perception System Calibration

The perception system requires intrinsic camera calibration and fiducial marker detection scaling. We used the *camera_calibration* ROS package [24] to obtain the intrinsic camera parameters including scale factor, focal length, pixel dimension, and distortion. Despite the intrinsic camera calibration, the translation estimation from *apriltag_ros* was found to be inaccurate in our implementation. To calibrate this fiducial marker detection process, we estimate a multiplicative factor between the fiducial marker displacement and manually measured displacement,

$$D = \sigma d \quad (11)$$

where D is the manually measured displacement, σ is the multiplication factor, and d is the displacement from fiducial marker detection.

To better estimate σ , we phrase an overdetermined system by sampling a number of displacement points along the linear shaft $\{d\}$,

$$\mathbf{D} = \sigma \mathbf{d} \quad (12)$$

where $\mathbf{D} = [D_1, D_2, \dots, D_N]^T$ is a vector of manually measured displacements, and $\mathbf{d} = [d_1, d_2, \dots, d_N]^T$ is a vector of fiducial marker displacements. The Moore–Penrose inverse is applied to solve the overdetermined system,

$$\sigma = \mathbf{D} \mathbf{d}^T [\mathbf{d} \mathbf{d}^T]^{-1} \quad (13)$$

We utilize the limit switches at the ends of the linear shaft (i.e., bed position calibration switches shown in Fig. 2) to facilitate the measurement of bed displacement. To start the perception system calibration, the bed moves to the left end until the left bed position calibration switch is triggered. At the same time, the fiducial marker detection at this position is recorded. Then the bed moves to the right end, triggering

the right calibration switch, and the fiducial marker detection is recorded. We input the manually measured length between the left and right calibration switches. During the perception calibration, we have a position controller that rotates the motor shaft by one angular step given one PWM signal. When the bed moves from one end to the other, we count and record the motor steps, from which the bed displacement per angular step (translational step resolution) is calculated. Then the bed randomly moves along the linear shaft to sample data points, such as step counts (from the left calibration switch) and fiducial marker detections. Using the step counts and translation step resolution, we calculate the actual bed displacements. The samples of the actual bed displacements and fiducial marker displacements are used in Eq. 13 to estimate σ .

B. Velocity Controller Calibration

The velocity controller calibration aims to reduce the uncertainties from the toothed belt transmission. Because of the closed-loop stepper motor, we assume that the actual angular velocity of the stepper motor is the same as the desired angular velocity. Given a desired translational velocity of the bed, Eq. 10 calculates the corresponding desired angular velocity. However, the toothed pulley radius r is close but not equal to the outside radius of the pulley. The uncertainty in r comes from factors such as the tightness of the toothed belt, manufacturing imprecisions, and tooth geometry. We correct for such uncertainty using a multiplicative factor,

$$\omega'(t) = \frac{\gamma v(t)}{r} \quad (14)$$

where γ is a constant that captures the first-order systematic uncertainty in the toothed belt transmission. The velocity controller calibration needs to estimate a γ that minimizes the error between the desired and actual translational velocities. We consider γ as a factor that calibrates velocity, and denote $\gamma v(t)$ as calibrated velocity. Instead of directly measuring translational velocity in real time, we conduct half-cosine displacement motions (i.e., $t = 1/(2f)$ in Eq. 6) and estimate γ from displacement differences,

$$D' = \gamma D \quad (15)$$

where D is the desired half-cosine displacement, and D' is the actual half-cosine displacement measured from the fiducial marker detection. Similarly, we randomly sample the half-cosine displacement motions and use the Moore–Penrose inverse to estimate γ . Using displacement difference to estimate velocity difference has the advantage of easy implementation. For example, we utilize the calibrated fiducial marker detection.

We briefly demonstrate that γ estimated from the displacements is the same multiplicative factor for velocity calibration. Based on Eq. 15, we have calibrated displacement function,

$$D'(t) = \gamma A - \gamma A \cos(2\pi ft). \quad (16)$$

where γ is estimated from the displacement differences described above. We take the derivative of $D'(t)$ and obtain

the calibrated velocity function,

$$v'(t) = \dot{D}'(t) = 2\pi\gamma Af \sin(2\pi ft). \quad (17)$$

We substitute Eq. 9 into Eq. 17,

$$v'(t) = \gamma v(t). \quad (18)$$

Therefore, γ estimated from displacements is also the factor that calibrates velocity.

VII. EXPERIMENTS AND RESULTS

We conducted experiments to demonstrate an application of the Shakebot in PBR fragility studies and to test its performance in validating simulation. These experiments focused on a PBR at the Double Rock site in coastal Central California [8]. The PBR, as shown in Fig. 6, was mapped by an unpiloted aerial vehicle and reconstructed using structure from motion and Poisson reconstruction algorithms [11].

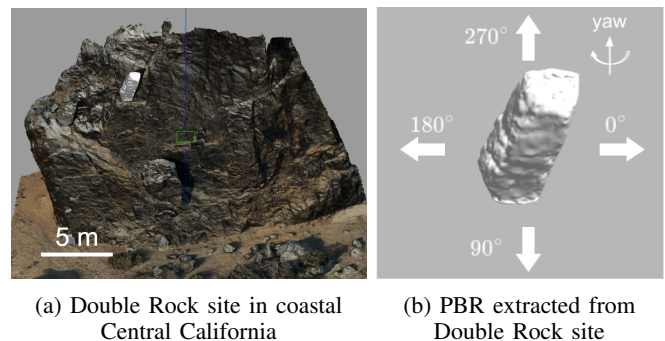


Fig. 6: Precariously Balanced Rock (PBR) at Double Rock site in coastal Central California. The yaw orientation indicates the relative direction of single-pulse cosine displacement motion.

The first experiment demonstrates the Shakebot application in studying the fragility anisotropy of PBRs. We down-scaled the Double Rock PBR from 151.0 cm to 12.0 cm and 3D-printed it with PLA material and a total mass of 105g, denoted as 3D-printed PBR(a). Because 3D-printed PBR(a) has asymmetric geometry, the overturning responses from different ground motion directions should be different. To verify such fragility anisotropy, we placed 3D-printed PBR(a) with two initial orientations (yaw angles of 0° and 270°) on the bed. Using the UI, we obtained the response diagrams from a set of ground motions, as shown in Fig. 7. The response diagrams show that 3D-printed PBR(a) oriented at a yaw angle of 0° is more fragile than at yaw angle of 270° . This result is consistent with analysis from the previous studies that PBRs with smaller minimal contact angle along the motion direction is more fragile [9, 25]. The resulting boundary curves have a similar pattern to the simulation results of the Double Rock PBR with original dimensions [11].

In the second experiment, we used the Shakebot to evaluate the overturning simulation. The Double Rock PBR was down-scaled to 12.8 cm and 3D-printed with the PETG material and a total mass of 404 g, denoted as 3D-printed

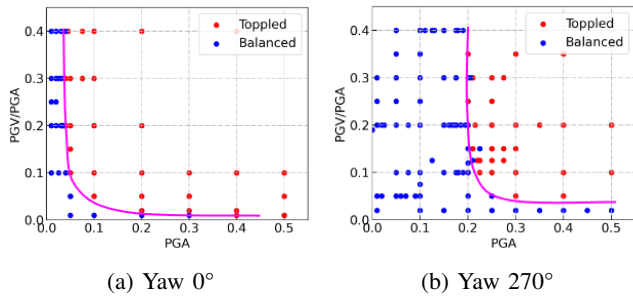


Fig. 7: Overturning response diagrams of the Double Rock PBR from orientations of yaw 0° and yaw 270° . The red and blue dots represent overturning responses of being toppled and balanced after single-pulse cosine ground motions, respectively. The curves indicate the boundaries of the overturning responses.

PBR(b). We imported the 3D model of the down-scaled PBR to Gazebo and conducted shake experiments using virtual shake robot [11]. to examine the simulation results, we used the Shakebot to overturn 3D-printed PBR(b). Both simulation and real-world experiments had the PBR orientation of yaw angle 0° . Fig. 8 shows that the overturning boundary curves from the real-world and simulation experiments are very close. Future work should explore the causes of their difference and possibly calibrate the virtual shake robot using the data from real-world experiments.

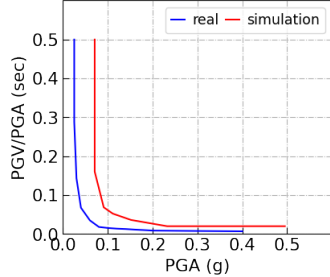


Fig. 8: Overturning boundary curves from Shakebot and virtual shake robot. Reprinted from [11]. Reprinted with permission.

Fig. 9 shows the result of velocity estimation by fusing the accelerometer data and fiducial marker detection. The regression model used the 3rd order polynomial function. We presented an offline method for velocity estimation, which is helpful for this study where the performance of the accelerometer is constrained by cost. The acceleration estimation can be improved with a better-quality accelerometer. Future work should also investigate real-time state estimation.

VIII. CONCLUSION

We introduced a low-cost, open-source shake table named Shakebot for ground motion seismic studies, specifically the overturning dynamics of PBRs for earthquake hazard analysis. Leveraging concepts and tools in robotics, we simplified

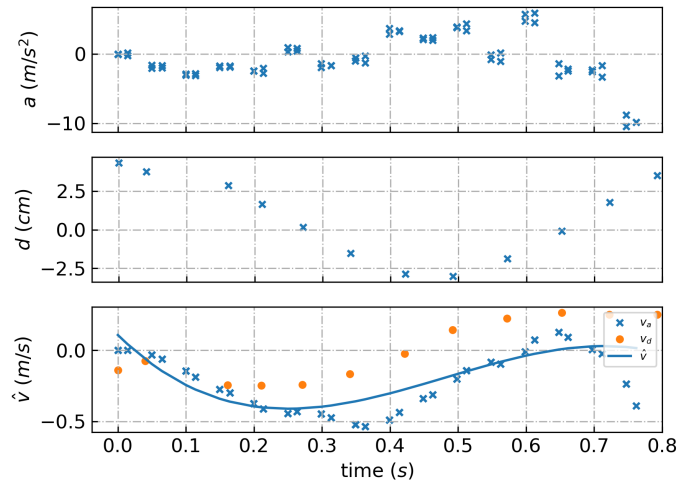


Fig. 9: Velocity estimation from regression of acceleration and displacement.

and advanced the hardware and software compared to the existing shake tables. We presented the technical details of the perception and motion systems, which are important for the open-source community to upgrade or customize the Shakebot. Experimental results showed the applications of the Shakebot for PBR studies. Our work demonstrates an interdisciplinary method of using robotics for natural sciences, providing a step towards robotics-enabled automated geoscience [11].

ACKNOWLEDGEMENTS

This research was supported by the Pacific Gas and Electric Company and Southern California Earthquake Center (Contribution No. 21137). SCEC is funded by NSF Cooperative Agreement EAR-1600087 and USGS Cooperative Agreement G17AC00047.

REFERENCES

- [1] L. S. Jacobsen. “Vibration research at Stanford university”. In: *Bulletin of the Seismological Society of America* 19.1 (1929), pp. 1–27.
- [2] X. Lu, G. Fu, W. Shi, and W. Lu. “Shake table model testing and its application”. In: *The Structural Design of Tall and Special Buildings* 17.1 (2008), pp. 181–201.
- [3] P. Harvey and C. Hibbard. “Enhancing the Undergraduate Civil Engineering Experience through 3D-Printing, Problem-Based Learning Opportunities”. In: *2022 ASEE Annual Conference & Exposition*. 2022.
- [4] J. N. Brune. “Precariously balanced rocks and ground-motion maps for southern California”. In: *Bulletin of the Seismological Society of America* 86.1A (1996), pp. 43–54.
- [5] B. Shi, A. Anooshehpour, Y. Zeng, and J. N. Brune. “Rocking and overturning of precariously balanced rocks by earthquakes”. In: *Bulletin of the Seismological Society of America* 86.5 (1996), pp. 1364–1371.
- [6] A. Anooshehpour, J. N. Brune, and Y. Zeng. “Methodology for obtaining constraints on ground motion from precariously balanced rocks”. In: *Bulletin of the Seismological Society of America* 94.1 (2004), pp. 285–303.

- [7] J. G. Anderson, G. P. Biasi, and J. N. Brune. “Precarious rocks: Providing upper limits on past ground shaking from earthquakes”. In: *Earthquake hazard, risk and disasters*. Elsevier, 2014, pp. 377–403.
- [8] A. Rood, D. Rood, M. Stirling, C. Madugo, N. Abrahamson, K. Wilcken, T. Gonzalez, A. Kottke, A. Whittaker, W. Page, et al. “Earthquake hazard uncertainties improved using precariously balanced rocks”. In: *AGU Advances* 1.4 (2020), e2020AV000182.
- [9] M. D. Purvance, A. Anooshehpour, and J. N. Brune. “Free-standing block overturning fragilities: Numerical simulation and experimental validation”. In: *Earthquake Engineering & Structural Dynamics* 37.5 (2008), pp. 791–808.
- [10] M. K. Saifullah and C. E. Wittich. “Seismic response of two freestanding statue-pedestal systems during the 2014 South Napa Earthquake”. In: *Journal of Earthquake Engineering* 26.10 (2022), pp. 5086–5108.
- [11] Z. Chen. “Automated Geoscience with Robotics and Machine Learning: A New Hammer of Rock Detection, Mapping, and Dynamics Analysis”. PhD thesis. Arizona State University, 2022.
- [12] W. Zhao, J. P. Queralta, and T. Westerlund. “Sim-to-real transfer in deep reinforcement learning for robotics: a survey”. In: *2020 IEEE Symposium Series on Computational Intelligence (SSCI)*. IEEE, 2020, pp. 737–744.
- [13] Z. Ding and H. Dong. “Challenges of reinforcement learning”. In: *Deep Reinforcement Learning*. Springer, 2020, pp. 249–272.
- [14] Quanser. *Quanser Shake Table II*. URL: <https://www.quanser.com/products/shake-table-ii/>.
- [15] T. Baran, A. Tanrikulu, C. Dundar, and A. Tanrikulu. “CONSTRUCTION AND PERFORMANCE TEST OF A LOW-COST SHAKE TABLE”. In: *Experimental Techniques* 35.4 (2011), pp. 8–16.
- [16] K. Educational. *Kelvin advanced earthquake simulator*. URL: <https://kelvin.com/kelvin-e-q-machine-2021/>.
- [17] E. Damcı and Ç. Şekerci. “Development of a Low-Cost Single-Axis Shake Table Based on Arduino”. In: *Experimental Techniques* 43.2 (2019), pp. 179–198. DOI: 10.1007/s40799-018-0287-5. URL: <https://doi.org/10.1007/s40799-018-0287-5>.
- [18] X. Shao and G. Enyart. “Development of a versatile hybrid testing system for seismic experimentation”. In: *Experimental Techniques* 38.6 (2014), pp. 44–60.
- [19] G. Kinay. “Construction and control of a desktop earthquake simulator”. MA thesis. İzmir Institute of Technology, 2006.
- [20] QUAKELOGIC. *Testbox-shaketable*. URL: https://quakelogic.net/actuators-shaketables/testbox_shaketable.
- [21] Quanser. *Quanser Shake Table I-40*. URL: <https://www.quanser.com/products/shake-table-40/>.
- [22] D. Malyuta. “Guidance, Navigation, Control and Mission Logic for Quadrotor Full-cycle Autonomy”. Master thesis. 4800 Oak Grove Drive, Pasadena, CA 91109, USA: Jet Propulsion Laboratory, Dec. 2017.
- [23] J. Wang and E. Olson. “AprilTag 2: Efficient and robust fiducial detection”. In: *2016 IEEE/RSJ International Conference on Intelligent Robots and Systems (IROS)*. IEEE, Oct. 2016, pp. 4193–4198. ISBN: 978-1-5090-3762-9. DOI: 10.1109/IROS.2016.7759617.
- [24] ROS.org. *camera_calibration*. URL: http://wiki.ros.org/camera_calibration.
- [25] D. E. Haddad, O. Zielke, J. R. Arrowsmith, M. D. Purvance, A. G. Haddad, and A. Landgraf. “Estimating Two-dimensional Static Stabilities and Geomorphic Settings of Precariously Balanced Rocks from Unconstrained Digital Photographs”. In: *Geosphere* 8.5 (2012), pp. 1042–1053.